







A pro-reparative bioelectronic device for controlled delivery of ions and biomolecules

Narges Asefifeyzabadi PhD¹  | Tiffany Nguyen MS¹ | Houpu Li PhD¹ | Kan Zhu PhD² | Hsin-ya Yang PhD³  | Prabhat Baniya PhD¹ | Andrea Medina Lopez BS³ | Anthony Gallegos BS³ | Hao-Chieh Hsieh PhD¹ | Harika Dechiraju PhD¹ | Cristian Hernandez MS¹ | Kaelan Schorger BS¹ | Cynthia Recendez BS² | Maryam Tebyani BS¹  | John Selberg PhD¹ | Le Luo PhD¹ | Elana Muzzy BS¹ | Cathleen Hsieh BS^{1,4} | Alexie Barbee BS¹ | Jonathan Orozco BA^{1,5} | Moyasar A. Alhamo MS³ | Michael Levin PhD⁶  | Elham Aslankoohi PhD¹ | Marcella Gomez PhD⁷ | Min Zhao MD, PhD^{2,3}  | Mircea Teodorescu PhD¹ | Roslyn Rivkah Isseroff MD^{3,8}  | Marco Rolandi PhD¹

¹Department of Electrical and Computer Engineering, University of California Santa Cruz, Santa Cruz, California, USA

²Department of Ophthalmology, School of Medicine, University of California Davis, Davis, California, USA

³Department of Dermatology, School of Medicine, University of California Davis, Davis, California, USA

⁴Department of Chemistry and Biochemistry, University of California Santa Cruz, California, Santa Cruz, USA

⁵Department of Economics, University of California Santa Cruz, Santa Cruz, California, USA

⁶Department of Biology, Tufts University, Medford, Massachusetts, USA

⁷Department of Applied Mathematics, University of California Santa Cruz, Santa Cruz, California, USA

⁸Dermatology Section, VA Northern California Health Care System, Mather, California, USA

Correspondence

Marco Rolandi, Department of Electrical and Computer Engineering, University of California Santa Cruz, Santa Cruz, CA 95064, USA.
Email: mrolandi@ucsc.edu

Roslyn Rivkah Isseroff, Department of Dermatology, School of Medicine, University of California Davis, Davis, CA 95616, USA.
Email: rriisseroff@ucdavis.edu

Funding information

Defense Advanced Research Projects Agency (DARPA), Grant/Award Number: D20AC00003

Abstract

Wound healing is a complex physiological process that requires precise control and modulation of many parameters. Therapeutic ion and biomolecule delivery has the capability to regulate the wound healing process beneficially. However, achieving controlled delivery through a compact device with the ability to deliver multiple therapeutic species can be a challenge. Bioelectronic devices have emerged as a promising approach for therapeutic delivery. Here, we present a pro-reparative bioelectronic device designed to deliver ions and biomolecules for wound healing applications. The device incorporates ion pumps for the targeted delivery of H⁺ and zolmitriptan to the wound site. In vivo studies using a mouse model further validated

Abbreviations: ACh, acetylcholine; AMPSA, 2-acrylamido-2-methylpropane sulfonic acid; GABA, gamma-aminobutyric acid; HPLC, high-performance liquid chromatography; H⁺, hydrogen ions; IEM, ion-selective membranes, ion-selective membranes; PCB, printed circuit board; PDMS, polydimethylsiloxane; PEGDA, poly (ethylene glycol) diacrylate; RE/CE, reference/counter electrode; WE, working electrode; Z+, zolmitriptan+.

Narges Asefifeyzabadi and Tiffany Nguyen contributed equally to this work.

This is an open access article under the terms of the [Creative Commons Attribution-NonCommercial-NoDerivs](https://creativecommons.org/licenses/by-nc-nd/4.0/) License, which permits use and distribution in any medium, provided the original work is properly cited, the use is non-commercial and no modifications or adaptations are made.

© 2024 The Author(s). *Wound Repair and Regeneration* published by Wiley Periodicals LLC on behalf of The Wound Healing Society.

the device's potential for modulating the wound environment via H^+ delivery that decreased M1/M2 macrophage ratios. Overall, this bioelectronic ion pump demonstrates potential for accelerating wound healing via targeted and controlled delivery of therapeutic agents to wounds. Continued optimization and development of this device could not only lead to significant advancements in tissue repair and wound healing strategies but also reveal new physiological information about the dynamic wound environment.

KEYWORDS

bioelectronic device, ion pumps, wound healing

1 | INTRODUCTION

Millions of people across the globe experience harmful impacts from both acute and chronic wounds.¹ In the United States alone, around 300,000 hospitalizations annually are linked to wounds.¹ Improved and innovative wound healing strategies are necessary to reduce the associated hospitalizations and healthcare costs.² Bioelectronic devices are one possible pro-reparative approach that bridges the gap between electronic control and complex biological processes like those of wounds.^{3,4} For example, recent bioelectronic developments use flexible or microfluidic platforms to deliver electric field stimulation to rodent skin wounds or in vitro scratch wound assays for accelerated healing.^{2,5} Other bioelectronic platforms incorporate the use of metal dots on polyester or cotton fibres to generate small potentials that are reported to aid in wound healing.⁶ Another bioelectronic approach involves utilising ion-selective membranes (IEMs) in devices to deliver specific ions and biomolecules to the wound site. An example of this kind of device is the electrophoretic ion pump.^{4,7} Ion pumps can deliver ions and biomolecules directly to a specific target, like the surface of a wound, in order advantageously alter the biological environment.^{8,9} This can result in promoting crucial cellular processes such as inflammation regulation, tissue regeneration and pain alleviation.^{10,11}

Recent studies demonstrated how bioelectronic ion pumps can deliver a range of ions such as K^+ ,¹² Ca^{2+} ,¹³ H^+ ,¹⁴ as well as neurotransmitters like acetylcholine (ACh),¹⁵ gamma-aminobutyric acid (GABA)¹⁶ and glutamate.¹⁷ These ion pumps typically deliver one therapeutic agent at a time. However, due to the complexity of the wound environment, simultaneous on-demand delivery of multiple agents could potentially enhance wound healing. To this end, our team has previously reported a bioelectronic electrophoretic ion pump capable of simultaneously delivering H^+ , Na^+ and Cl^- ions.¹⁸ Notably, the localized delivery of inorganic ions has the potential to alter the ionic microenvironment at wound sites, significantly impacting the healing process.¹⁹ For example, acidic environments foster the growth of new tissue and prevent bacterial infections²⁰ in addition to stimulating the production of collagen, fibronectin and other proteins essential for wound healing.²¹ pH changes resulting from proton delivery could also contribute to the overall therapeutic effects through the modulation of cell migration and macrophage

polarisation.^{22–25} Ca^{2+} and K^+ are involved in wound healing, but whether the direct application of these ions to wounds is useful remains a question without a simple straightforward answer. Ca^{2+} plays an important role in wound healing by regulating different processes such as coagulation, inflammation, angiogenesis, apoptosis, epithelization and migration of cells. Ca^{2+} ions can also be released by damaged cells.²⁶ Meanwhile, K^+ is involved in the regulation of cell migration and proliferation mainly via the mechanisms of regulating membrane potentials and ionic environment of wounds, both of which are essential for wound healing.²⁶ Some studies show that blocking K^+ channels with drugs or high concentrations of KCl can enhance wound healing in vitro and in vivo, but the spatiotemporal dynamics of Ca^{2+} , K^+ and other ions contribute to sophisticated mechanisms for ionic involvement in wound healing.

Further, literature indicates that certain neurotransmitters also have pro-reparative effects. In mice, it has been demonstrated that agonists for the gamma-aminobutyric acid (A) (GABA) receptor improve maturation of the re-epithelializing epidermis.²⁷ Topical application of GABA likewise improved healing in rat skin wounds and increased the dermal generation of pro-reparative cytokines FGF and PDGF.²⁸ Since glutamine can be used as a precursor for proline synthesis, and proline is a main component of collagen, a number of studies have demonstrated that parenteral supplementation with glutamate improves healing.²⁹ Particularly relevant to our delivery device is the finding that wound dressings that incorporate glutamic acid promote improved wound re-epithelialization and enhance collagen generation the dermis. Treatment also accelerated vascularization of the wounds.^{30,31} Further, the findings that keratinocytes express receptors for acetylcholine, and that their activation modulates cell migration and proliferation, prompted a study on application of low doses of ACh to mouse skin wounds. Topical ACh administration resulted in faster wound re-epithelialization and earlier appearance of wound healing markers (eg MMP9) that in other protocols.³²

Serotonin also plays a role in wound healing by increasing cell viability and proliferation.³³ In a frog (*Xenopus laevis*) model, ectopic application of serotonin following eye surgery strongly improved the degree of innervation,³⁴ which directly affects wound healing.³⁵ However, serotonin is a labile molecule and easily degraded in vivo; thus, we can mimic endogenous serotonergic signalling with a more stable

exogenous molecule of receptor type 1B,D that has neurotrophic effects.³⁶ The selective serotonin 1B and 1D receptor agonist, (S)-4-[[3-[2-(dimethylamino)ethyl]indol-5-yl]methyl]-2-oxazolidinone (zolmitriptan) is one such reagent that is well-known and human-approved. The anti-inflammatory and pain-reducing properties of zolmitriptan and its ability to promote angiogenesis and modulate neurogenic reactions make it a promising pro-reparative candidate.^{37,38} Research on migraines and meningitis shows that zolmitriptan reduces inflammation and vasodilation by inhibiting the release of pro-inflammatory neuropeptides from nerve fibres.³⁷ Because zolmitriptan is a selective 5-hydroxytryptamine 1B/1D receptor agonist, it can activate serotonin receptors in the skin with downstream effects on **keratinocyte migration and wound inflammation**.^{33,39} Zolmitriptan thus exhibits significant pro-reparative potential, particularly considering the vital role of these mechanisms in the wound healing process.

Building on these investigations, here we introduce an advanced bioelectronic device with the capacity to co-deliver ions, such as H^+ , alongside protonated biomolecules like zolmitriptan (Figure 1). Through our research, we demonstrate that precise dosage control is achievable by managing the flux of charges. Furthermore, all cations and protonated biomolecules were driven by electrical currents, which have been proven to be able to modulate various cell behaviours, such as cell migration, proliferation and differentiation.^{40–48} Here, we propose a new approach involving an electrical mechanism combined

with ion/biomolecule delivery for wound healing. Though demonstrated to benefit wound healing, the specific healing mechanisms influenced by electrical currents and cation delivery are not yet fully understood and remain largely unexplored in terms of therapeutic timing effects. To this end, as well as to validate the bioelectronic device's practical application with other biomolecules, we conduct an *in vivo* study using a mouse wound model (Figure 1).

2 | RESULTS AND DISCUSSION

The design of the bioelectronic device enables electronically programmable ionic and biochemical delivery to biological targets. In our study, we used wounds in a mouse model as the target (Figure 1A). The fabrication process of the device involves several steps, starting with the creation of 3D printed moulds to form a two-layered polydimethylsiloxane (PDMS) body. PDMS is a flexible and biocompatible polymer commonly used in the fabrication of medical devices.^{49,50} The top layer of the PDMS body contains reservoirs (Figure 1B, left and middle) that hold cationic therapeutics in aqueous form, such as hydrogen ions (H^+) or protonated biomolecules such as zolmitriptan⁺ (Z^+). To achieve controlled delivery of ions and biomolecules, the PDMS body integrates with a custom printed circuit board (PCB) (Figure 1B, right).⁵¹ The PCB serves as the control system for the device, allowing for programmable delivery of the therapeutic.

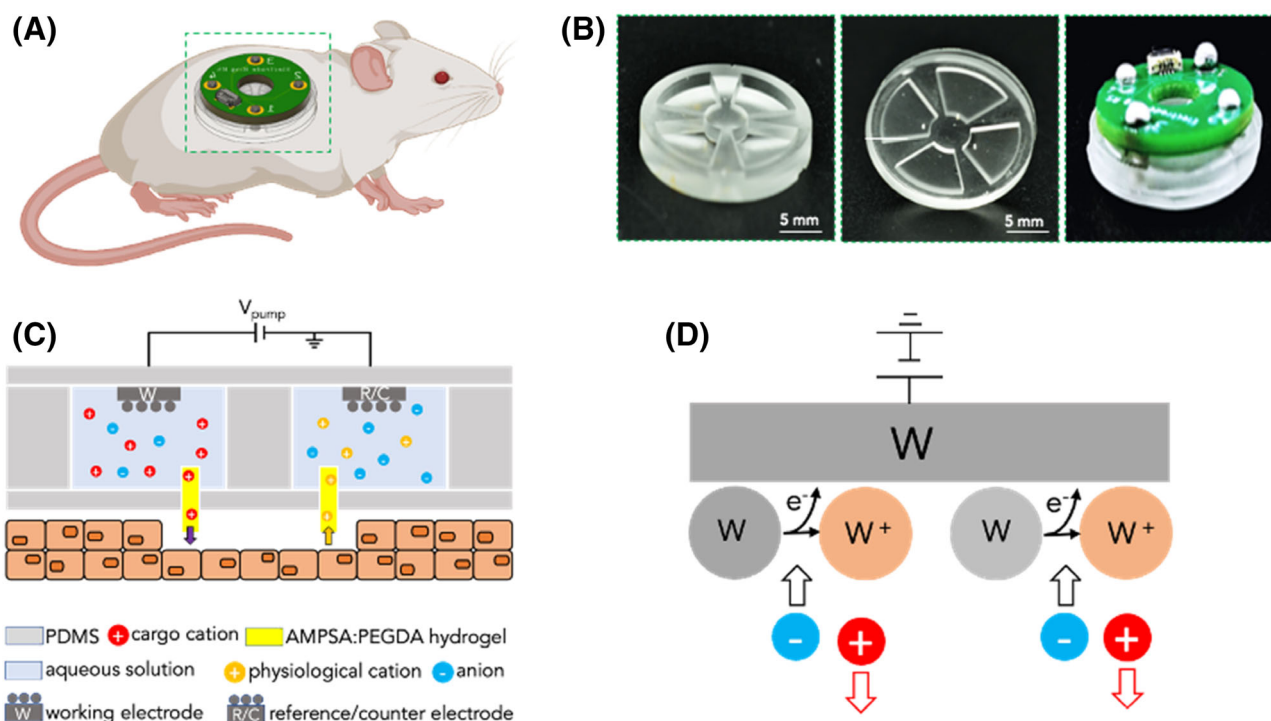


FIGURE 1 (A) The schematic of the bioelectronic device demonstrates its application in a mouse model. (B) The bioelectronic device consists of a 3D printed PDMS body featuring four reservoirs for solution storage. The body is securely bonded with a PDMS lid and integrated with a printed circuit board (PCB). (C) Schematics of the ion pumping process illustrate how the electric field drives protons towards the target through the ion-selective hydrogel (yellow). (D) The generalised electrochemical reaction for the ion pump WE. The schematic illustrates the voltage-induced oxidation mechanisms which facilitate proton conduction.

The device achieves ion and biochemical delivery via ion pump technology. The working mechanism of ion pumps is to deliver charged species from the source reservoir, through the IEM and to the target (Figure 1C). This transport occurs by applying a low voltage (V_{pump}) between the working electrode (WE) and the reference/counter electrode (RE/CE). V_{pump} drives the protonated ions or biomolecules across the IEM. In this context, the ions or biomolecules include H^+ and protonated zolmitriptan $^+$, and V_{pump} corresponds to the delivery of each, represented as V_{H^+} or V_{Z^+} . Each reservoir of the device houses a metal wire that acts as a WE or RE/CE. Further, the aqueous solution in each reservoir interfaces with hydrogel that acts as the IEM in our system. The hydrogel contains 2-acrylamido-2-methylpropane sulfonic acid (AMPSA) and poly (ethylene glycol) diacrylate (PEGDA) and is selective to cationic species.⁵² Thus, the ion pump selectively permits the passage of protonated ions and biomolecules while preventing the passage of anionic species. The substance in the reservoir thus must be naturally positively charged or protonated through the use of an acidic solution. When V_{pump} is positive, cationic species from the reservoir at the WE electrophoretically transfer into the target through the IEM. This is due to oxidation reactions that occur at the WE (Figure 1D). To maintain charge neutrality, physiological cations exit the wound and enter the opposite reservoir at the RE/CE. These physiological cations also serve as the charge carriers at the wound surface, thereby completing the circuit.

In order to deliver specific ions and biomolecules (H^+ and protonated zolmitriptan $^+$), we use four glass capillary fibres to house the cation-selective IEM. We insert the IEM-filled capillaries into the PDMS device where they can interface with the wound (Figure 2A,B). A zoomed-in optical microscope image reveals the openings of the capillary tubing and provides a visual of the bulk hydrogel (Figure 2C). The IEM, previously reported in our work,⁵² is a cross-linked polyelectrolyte hydrogel made selective to cations through the presence of fixed negative charges within the polymeric network. This selectivity is achieved through a hydrogel polymerisation reaction, where AMPSA acts as the monomer, and PEGDA acts as the cross-linker in the presence of a UV photoinitiator. The hydrogel-filled capillaries require a preparation procedure that we have previously optimised.⁵²

To evaluate the device's performance, we utilised a fluorescence microscope (Keyence BZ-X710) setup and an indicator dye for H^+ detection (Figure S1). We first placed the devices on a 200- μL target solution containing buffer along with the indicator dye. Next, we used a V_{H^+} pulse with a positive cycle at 1 or 2 V across the WE and RE/CE of each device for several minutes. V_{H^+} enables the electrophoretic transfer of cations from the device reservoir (at the WE), through the IEM and into the target solution. Concurrently, pre-existing cations in the target solution migrate through the IEM to the other reservoir (at the RE/CE). The observed changes in fluorescence intensity within the target solution corresponded to variations in ion concentration. On the other hand, the delivery of cationic biomolecules such as zolmitriptan required the use of high-performance liquid chromatography (HPLC) rather than fluorescence microscopy.

The underlying principle of the device remained unchanged, as a positive V_{Z^+} transfer protonated zolmitriptan $^+$ from the reservoir to the target solution containing NH_4Cl . We maintained the same device setup, excluding the microscope (Figure S2).

For H^+ delivery, we used platinum (Pt) as the WE (Figure 3A). By using Pt as the WE, chloride ions present in the acidic solution undergo an initial reaction with Pt, resulting in the formation of PtCl_4^{2-} .^{53,54} This newly formed PtCl_4^{2-} species can subsequently undergo further reactions with additional chloride ions in the solution, leading to the formation of PtCl_6^{2-} .^{53,54} Based on the standard redox potentials, the energy required for the formation of PtCl_4^{2-} and PtCl_6^{2-} is lower compared with the energy needed for the process of water-splitting.⁵⁵ This indicates that the formation of PtCl_4^{2-} and PtCl_6^{2-} are favoured and occur prior to any water-splitting reactions taking place.^{54,55} Furthermore, with the consumption of each chloride ion, one proton is pushed through the IEM.⁵⁴ For detecting $[\text{H}^+]$, the target solution comprised tris buffer and 5-(and-6)-Carboxy SNARF $^{\text{TM}}$ -1, a pH indicator dye with emissive wavelengths at 580 nm and 640 nm.

Ratiometric calibration of the fluorescence response at both wavelengths, using solutions of known $[\text{H}^+]$, facilitated pH determination. Employing a device containing 0.5 M HCl in the reservoirs, we alternated V_{H^+} pulses (+1 and -1 V), with positive pulses lasting

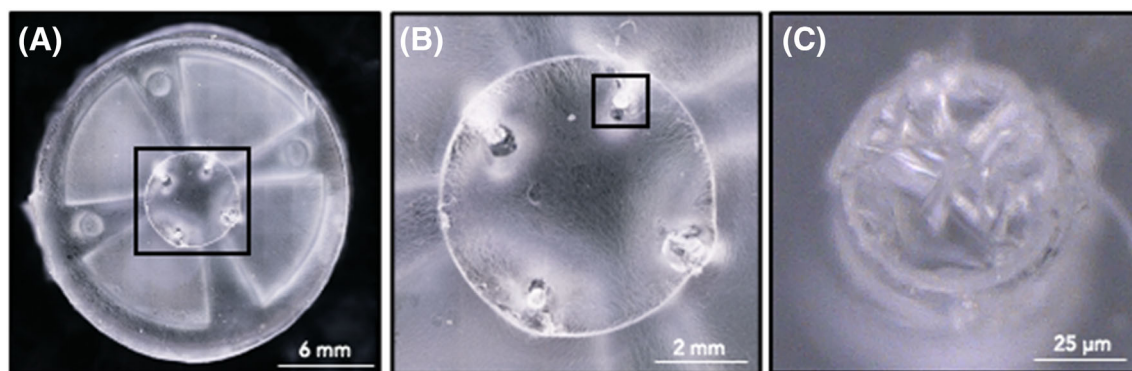
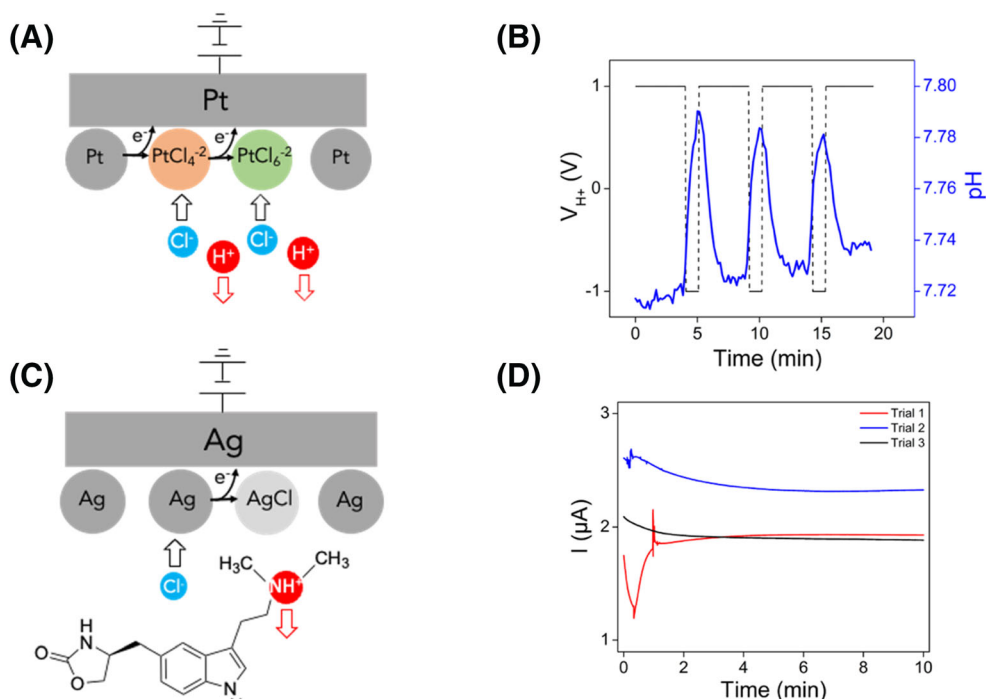


FIGURE 2 (A) An optical microscopy image of the wound-interfacing side of the device. (B) Zoomed-in image revealing the wound-interfacing PDMS and the openings of the capillary tubing filled with hydrogel. (C) A microscopy image of the bulk hydrogel within the glass capillary fibre.

FIGURE 3 (A) The oxidation reaction that occurs at the WE in HCl solution when Pt is the electrode material. (B) pH change, calculated using SNARF dye, changes over time in response to V_{H^+} . (C) The oxidation reaction that occurs at the WE in Zolmitriptan-HCl solution when Ag is the electrode material. (D) Current response of the device to an applied 2-V voltage, measured across three different trials.



4 min and negative pulses lasting 1 min. The positive V_{H^+} pulses transferred H^+ from the device reservoir to the target solution, resulting in fluorescence intensity changes at both emissive wavelengths (Figures S3 and S4), and corresponding pH change near the outlet of the capillary at the WE (Figure 3B). Figure S5 shows fluorescence microscopy calibration images taken for the SNARF dye, and Figure S6 depicts the fluorescence intensity trends at 580 and 640 nm for calibration.

For proton delivery calculations, we consider a local target volume of 1 μL . Since the port size of the hydrogel capillary is 0.1 mm, we assume the target (a wound bed for in vivo applications) to be humid with a <1 mm layer of liquid. We calculated a 1-mm³ volume, equivalent to 1 μL , and accounted for subsequent drug absorption and metabolism. While a standard practice is absent in this field, we used this rough estimation to demonstrate concentration for comparison with other topical application. We thus used this 1- μL volume for initial device characterization as well. With each positive V_{H^+} pulse, the proton delivery device decreased pH by approximately 0.03 to 0.05 units. Considering the buffering capacity of the target solution, we determined that the average per-pulse delivery efficiency¹² for three positive pulses was $41.2\% \pm 11.3\%$. Table S1 presents the pH change per pulse and per second for the device in Figure 3B, as well as an additional device in Figure S7. We have also previously demonstrated successful ion delivery using similar bioelectronic devices for H^+ , K^+ and Na^+ in vitro.^{12,18}

To demonstrate the potential of the bioelectronic device for biomolecule delivery, we performed similar delivery tests using the selective serotonin receptor agonist zolmitriptan. Zolmitriptan was dissolved in 100 mM HCl solutions at 1:1 molar ratio to form protonated zolmitriptan⁺ (Z^+). For Z^+ delivery, we used Ag as the WE (Figure 3C). With a positive V_{Z^+} pulse, Cl^- undergoes oxidation to

become Cl , resulting in the formation of $AgCl$ on the Ag surface. Simultaneously, Z^+ electrophoretically transfers through the IEM towards the target solution. With a V_{Z^+} of 2 V for 10 min trials, we recorded the current response of three devices. To determine the delivery efficiency, we then conducted calibration using solutions with varying concentrations of Z^+ and performed analysis using High-Performance Liquid Chromatography (HPLC).

For Z^+ delivery, the total drug loaded in the device reservoir is 3.915×10^{-6} mol. As the amount of zolmitriptan delivered through the ion pump is very small compared with the amount loaded in the device, the concentration change in the source reservoir would also be very small. Measuring the source solution is thus neither a practical nor accurate analysis method. To quantify the Z^+ concentration delivered, we collect samples from the target/receiving solution and analyse them using HPLC (calibration plot shown in Figure S8). The total electrical charge delivered by the system, measured as current, can be calculated by integrating current over time. In the hydrogel, this charge is carried by charge carriers (Z^+ and other cations in solution), so the amount of Z^+ measured via HPLC is directly proportional to the total charge.

The current thus serves as a reliable indicator of Z^+ delivery in real-time. By comparing the mole number of delivered Z^+ with the mole number of electrons, we determined that the charge carrier efficiency for zolmitriptan delivery is $18.8\% \pm 11.1\%$ considering three trials of a good device (Figure 3D and Table S2). This means that for every 100 electrons passing through the circuit, approximately 18 Zolmitriptan molecules transfer to the target solution. Subsequently, we can apply this efficiency to calculate zolmitriptan delivery in vivo, a well-established method in the field of ionic drug delivery.^{56,57} Table S3 shows the efficiencies of three devices actuated for three 10-min trials using a 350- μL target solution of 50-mM NH_4Cl .

As the results demonstrate, at times we find that “bad” devices leak or diffuse excessive zolmitriptan due to defects in the hydrogel, which results in high efficiencies. This issue could be resolved in the future using a Donnan layer,⁵⁸ which would help prevent leakage via diffusion and ensure better electronic control of delivered dosage.

As observed in Figure 3D, device performance exhibits variations in terms of magnitude, which we believe are related to the contact resistance of the hydrogel-target interface. Optimising these factors to reduce performance variation may be impractical due to natural variation of in vivo environments. Nevertheless, the devices are capable of delivering ions and drugs, and the amount of drug delivered can be determined by the electrical current and charge from the system. In the future, we plan to implement a more advanced closed-loop control system that would compensate for devices with lower current by applying a higher V_{pump} and longer delivery time to achieve the same dose.

Prior to using these bioelectronic devices for in vivo therapeutic delivery, we conducted thorough biocompatibility assessments to ensure that all materials in direct contact with the wound bed had no adverse biological effects (Table S4). We then assessed the device's ability to deliver ions and biomolecules in a mouse model. For each in vivo study, we used three mice. Each mouse had one circular 6-mm splinted excisional wound (Figure S9). Since wound contraction is a

significant aspect of wound healing in mice but not in humans, we employed a silicone splint ring to minimise its impact during the study.⁵⁹ Then, we positioned the bioelectronic device onto the silicone splint ring (Figure 4A). The distance between the device and the wound bed/surface was approximately 1 mm. We specifically designed a 1 mm thickness notch at the bottom, aligning with the depth of the wound bed, to ensure direct contact between the wound fluid and the ion-selective membrane (IEM). This design feature enhances the efficacy of delivering therapeutic ions and biomolecules directly to the wound site.

We first tested the in vivo capability of our device to deliver large therapeutic biomolecules such as Z^+ . Previous studies have demonstrated that directly administering zolmitriptan to the human skin alleviates pain, reduces inflammation and promotes the formation of new blood vessels.³⁸ We monitored the device's current response to a 2-V peak-to-peak rectangular wave while on a mouse wound. The waveform consisted of 60 s at 2 V and 30 s at 0 V (Figure 4B). Based on the efficiency determined from our previous characterisation, the estimated concentration of zolmitriptan delivered to the wound surface was $0.518 \text{ mM} \pm 0.524 \text{ mM}$ when considering a local wound fluid volume of $1 \mu\text{L}$ (Table S5). This was achieved by three devices that delivered on average $2.66 \times 10^{-4} \text{ C} \pm 2.68 \times 10^{-4} \text{ C}$, or maintained a current of $2.2 \mu\text{A} \pm 2.2 \mu\text{A}$ for 2 min. The large current variation

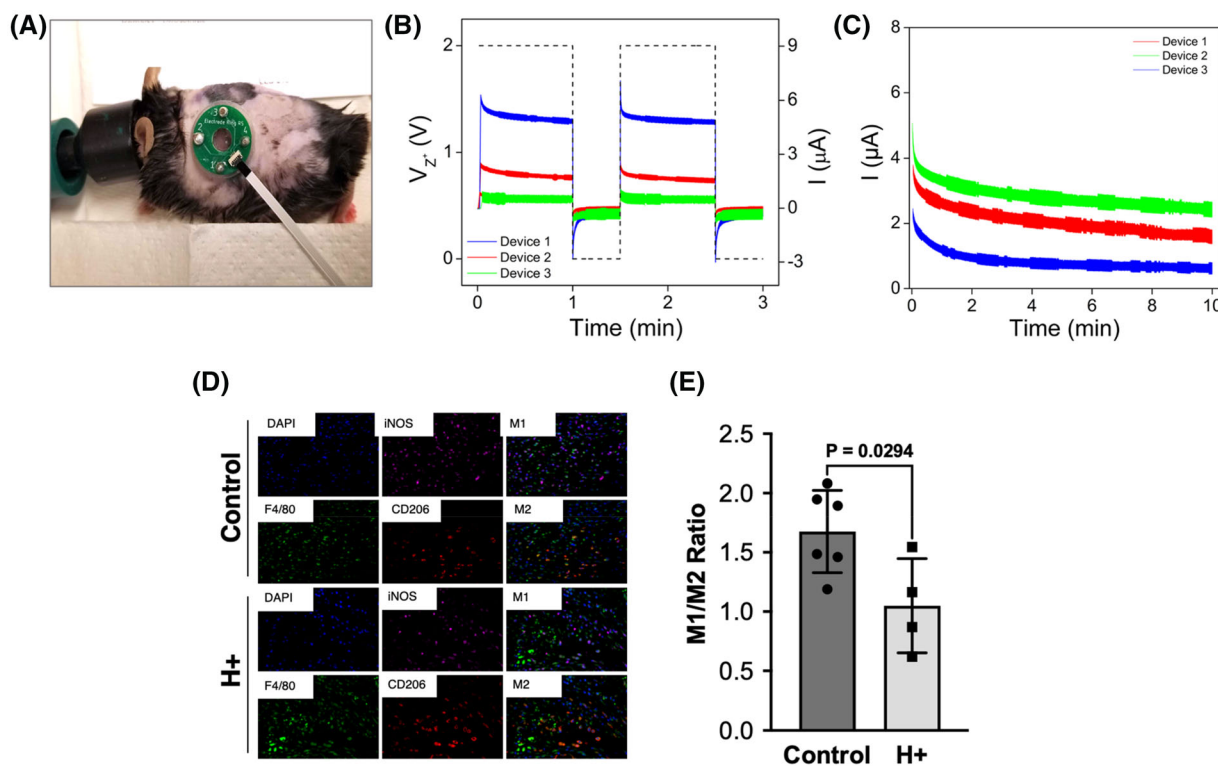


FIGURE 4 (A) Setup of the bioelectronic device on a mouse wound. The current profiles obtained from the actuation of the respective devices on anaesthetised mouse wounds for (B) Zolmitriptan⁺ and (C) H^+ delivery. (D) Representative immunofluorescence images of dorsal skin wound tissues from mice 3 days after wounding with/without H^+ treatment. Seven- μm thick tissue sections were co-stained with F4/80 (green) plus iNOS (purple), CD206 (red) and DAPI (blue) as indicated. $n = 6$ mice for the control, and $n = 4$ for the H^+ treated group. 5 images were taken for each sample for quantification. (E) Quantification of M1/M2 macrophage ratios from H^+ delivery experiments ($p = 0.0294$). Dots in the floating bars indicate data from each mouse with lines showing the mean values.

exhibited in these proof-of-concept devices could again benefit from future utilization of closed-loop control. Though zolmitriptan has several pro-reparative effects, it is not widely used for wound healing and thus no clinical data exist regarding an ED50 value for topical wound application. However, Blackiston et al. reported that 50 μM of Zolmitriptan promotes nerve growth in tadpoles.³⁶ Considering a target volume of 1 μL , delivery of this zolmitriptan concentration using our devices could be achieved within 82 s or less (Table S5). These experimental findings validate the successful delivery of Z^+ to a mouse wound using our bioelectronic device.

As previously stated, H^+ ions hold potential implications for improving healing via modulation of both innervation and macrophage recruitment.^{60,61} Using the established mouse model, we conducted a control experiment and an actuated device testing experiment. The control experiment involved plain PDMS device bodies with capillaries (without PCBs) and unfilled reservoirs, while the actuated device testing involved devices with attached PCBs and reservoirs filled with 0.5-M HCl. We recorded the current profiles obtained from three different devices during a daily 10-min actuation period with a constant V_{H^+} of 2 V (Figure 4C). We note that the administered pulses differed between the in vitro and in vivo experiments due to limitations with actuation time on the mouse model. For in vitro characterisation, the use of positive and negative V_{H^+} pulses aided in characterising the delivery capabilities of the device during positive V_{H^+} application (the normal operation of the device) and negative V_{H^+} application (only used for efficiency characterisation purposes). The version of the device used for these experiments requires a wired power supply. Thus for in vivo experiments, the normal operation could only occur during limited anaesthesia time so as to not restrain the mouse movement.

Assuming an efficiency of 41.2%, we estimate that the three devices delivered an average of 4.9 ± 2.6 nanomoles of H^+ , achieved by an average steady-state current of $1.88 \mu\text{A} \pm 0.99 \mu\text{A}$ (Table S6). This device is therefore not likely to achieve large pH changes in the bulk of large wounds, as it delivers a nanomole proton dosage. This estimation provides valuable insights into the device's capability to deliver H^+ ions, facilitating further analysis and interpretation of its potential pro-reparative effects⁶¹ and related biological processes.⁶² Several studies exist regarding the pro-reparative effects of acidic pH, but the exact mechanisms by which acidification affects wound healing mechanisms on a cellular level remain largely unexplored given the complexity of wound healing.²⁴ Bacterial growth in infected wounds is inhibited by a pH less than 6, while antimicrobial activity has been shown to drop at pH 5.5.²¹ Low wound pH also increases protease degradation, allows for optimal hyaluronidase activity, increases fibroblast proliferation and promotes keratinocyte differentiation among others.⁶¹ Even so, the process of wound healing maintains an intricacy such that the effects of pH itself are still inconclusive across separate studies.²² There is therefore a need to further study the affects of acidic pH on wound healing efficacy and biological mechanisms, and our device addresses this necessity.

Further, pH nanodomains at both the intracellular and extracellular level modulate components involved in cell migration,²³ an active

component of wound healing. Our device is able to modulate pH at this small scale and could facilitate further studies of the effects of such localised pH changes. Additionally, our device generates electric fields as it delivers protons and thus exerts electrical effects on cells in the wound bed. Such electric fields affect cell migration, proliferation and differentiation/phenotype modification that play a role in wound healing.⁶³ As previously noted with in vitro delivery, the current curves depicted in Figure 4B,C demonstrate wide variations in magnitude largely attributed to the resistance of the wound and the contact interface, which varies with in vivo samples. This variation could be compensated for by applying a closed-loop system, a feature that would also allow for the study of pro-reparative mechanisms that occur with various proton dosages at different wound healing stages.

To investigate the biological effects of our bioelectronic system in vivo, we employed immunohistochemistry (IHC) staining to study the presence and distribution of macrophages in wounded skin samples with 3 days of H^+ treatment. This entailed a treatment protocol in which we positioned the H^+ delivery devices on each mouse and activated them daily over 3 days. Specifically, the ion pump was actuated for a duration of 10 min during each treatment session. Macrophages play crucial roles in various aspects of wound healing and are among the initial cell types that migrate to the wound site. It is worth noting that macrophages exhibit significant plasticity and can transition between different phenotypes.⁶⁴ In vitro studies have demonstrated the transition from the classically activated M1 macrophage (pro-inflammatory phenotype) to the alternatively activated M2 macrophage (anti-inflammatory phenotype) known for promoting tissue repair.^{40,65} M1 macrophages secrete cytokines such as IL-1, TNF α , IL-6, IL-12 and matrix metalloproteinases (MMPs), while M2 cells produce arginase, TGF β , CCL18, PGE2, and IL-10 and upregulate scavenger receptors such as CD206 and CD163.⁶⁴ However, in the in vivo environment, macrophage phenotype transition may exist as a continuum rather than a strict dichotomy, influenced by various signals within the microenvironment.⁶⁶ Therefore, the function of macrophages undergoes precise regulation and dynamic changes in both temporal and spatial dimensions.

In this study, our focus was to assess the relative distribution of the two predominant macrophage phenotypes, M1 and M2, at the wound site three days post-wounding. Day 3 was chosen with the goal of analysing if treatment successfully shortened the inflammatory phase and initiated the proliferation phase earlier in the wound healing process. The inflammatory phase is indicated by high M1, and low M2, whereas the proliferation phase is indicated by a decrease in M1 and an increase in M2.^{66,67} Previous experiments show that the M1/M2 ratio starts to change in Days 4–7 of the normal wound healing process.^{68,69} To test whether our treatment shortens the inflammatory phase, that is, to bring forward the time of changes in M1/M2 (decrease in M1, increase in M2), we thus reasoned that Day 3 would be an appropriate time point to perform macrophage analysis of various treatments compared with the non-treatment control.

Data were collected from two control mice and four mice treated with H^+ . To distinguish M1-like cells, we employed iNOS as a specific

marker, while CD206 was used to identify M2-like cells. Additionally, a pan macrophage marker, F4/80, was co-stained to facilitate the overall macrophage visualisation and analysis. Representative images illustrate that macrophages of both phenotypes were observed in the wound bed of all samples (Figure 4D). The wounds that received H^+ treatment exhibited a decrease in the quantity of F4/80+iNOS+ M1 macrophages, while the number of F4/80+CD206+ M2-like cells showed minimal change in comparison. Consequently, the ratio of M1 to M2 macrophages decreased noticeably after three days of treatment (Figure 4E). These results indicate that H^+ stimulation using our bioelectronic bandage can modulate the wound environment, thereby expediting the healing processes via shortening of the inflammatory phase and bringing forward the proliferation phase.

As stated, the duration of this experiment was limited to 3 days. This timeframe was specifically chosen to examine the shift in M1/M2 ratio at the point when M1 peaks in untreated wounds. However, this early timepoint may not capture prominent changes in wound closure. Our analysis revealed no statistically significant differences in wound re-epithelialization at day three between treated and control wounds. However, we acknowledge the importance of long-term follow-up, and in our future works, we plan to conduct experiments with extended durations to further elucidate the effects of our bioelectronic device on wound healing. Nonetheless, our findings offer valuable insights into the potential roles of macrophages in response H^+ treatment and its therapeutic effects.

3 | CONCLUSION

We developed a pro-reparative bioelectronic device for controlled delivery of therapeutic ions and biomolecules towards facilitating wound healing. Our advanced, bioelectronic ion pump-based device enables targeted delivery of therapeutic agents to the wound site. The use of electrophoretic ion pumps and ion-selective hydrogels allows for the flow-free delivery of specific ions such as H^+ as well as biomolecules like zolmitriptan. The successful delivery of these substances was validated through in vitro characterisation. Further, the in vivo studies conducted in a mouse model demonstrated the device's potential in wound healing, as shown through the decreased M1/M2 macrophage ratio observed with proton delivery.

This bioelectronic device holds promise for addressing the complex physiological changes that occur during wound healing. By delivering therapeutic treatment in a targeted manner, the device has the potential to decrease inflammation and stimulate tissue regeneration, thereby enhancing the healing process. The incorporation of two source reservoirs in each device facilitates future use of this device for simultaneous delivery of different ions or drugs. Further optimization and development of this device, including exploring additional ions and biomolecules, could lead to innovative timing-based strategies for wound healing and contribute to improved patient outcomes.

Though implementation of closed-loop control would account for performance variability in our devices, we acknowledge that the size of the IEM and solution reservoirs would need to be increased to

reach significantly higher dosages on larger wounds. Other potential issues with scaling up the device for human therapies may arise due to differences in skin anatomy between mice and humans. It is possible that the effectiveness of the device will be limited by differences in skin thickness and sweat gland density. Additionally, differences in skin sensitivity could lead to irritation and discomfort when using the device. Therefore, the size of the device, the concentration of therapeutic agents delivered, and the overall effectiveness may need to be adjusted to accommodate the larger and structurally distinct human skin. However, the principles of ion and therapeutic delivery demonstrated in the study could still apply to human therapies, though further research and device refinement would be necessary to ensure efficacy and safety in a human context. Considering this, the integration of bioelectronics with wound healing processes represents a promising avenue for future research and the development of advanced therapeutic approaches.

4 | METHODS

4.1 | Hydrogel capillary fibres fabrication

We have reported the fabrication process for hydrogel capillary fibres in previous work.⁵² The hydrogel precursor solution comprises 2-acrylamido-2-methyl-1-propanesulfonic acid (AMPSA) (1 g, M), polyethylene glycol diacrylate (PEGDA) (1071.41 μ L, 0.4 M), and photoinitiator (I2959) (0.05 g, 0.05 M). We first treat a glass capillary fibre (ID 100 μ m, OD 375 μ m, 10-cm long) with NaOH etching and silane A174 to promote covalent bonding between the hydrogel and glass fibre interior. After injecting the hydrogel precursor solution into the fibre, UV cross-linking occurs for five minutes at 8 mW/cm². We then cut the capillary fibres into 5-mm pieces and store the fibres in solution for several hours before ionic conductivity measurement and device integration.

4.2 | Ionic conductivity measurement

When measuring ionic conductivity of the hydrogel capillaries outside the device, we use PDMS wells to separate two electrolyte solutions, each interfacing with an electrode. One 5-mm hydrogel capillary connects across both solutions. We then use an Autolab potentiostat PGSTAT128N with analytic software Nova 2.0 to supply a voltage across the electrodes and measure the resultant current. Measurement of device current entails a similar process using the electrodes inside the device.

4.3 | Fluorescence probes

For detection of H^+ concentration, we used real-time imaging on a fluorescence microscope (Keyence BZ-X710) with fluorescence probes. We achieved pH detection with the fluorescent probe 5-(and-6)-Carboxy SNARF™-1 (C1270, Invitrogen™), which exhibits a

$\lambda_{\text{excitation}}$ between 488 and 530 nm and a dual $\lambda_{\text{emission}}$ at 580 nm and 640 nm. The ratio of the fluorescence intensities at both wavelengths factors into pH determination. The concentration of SNARF in the target was 50 μM in 0.1 M tris buffer. All fluorescence images were analysed using ImageJ.

4.4 | M1/M2 immunohistochemical (IHC) staining

At the conclusion of each experiment, mice were euthanized and their wounds were excised. Wound tissues were fixed in a 4% paraformaldehyde solution for 24 h. Subsequently, the fixed tissues underwent processing in a Tissue-Tek VIP 6 processor (Sakura Finetek, Torrance, CA) and were embedded in paraffin wax blocks. To facilitate analysis, the tissues were then sectioned into 5- μm thick slices and mounted onto glass slides. For macrophage identification, wound tissue slices underwent antigen retrieval treatment and were subsequently blocked for 2 h using 10% Donkey Serum (Thermo Fisher). Following that, the samples were incubated overnight with primary antibodies targeting specific markers: F4/80 (dilution 1:50; MCA497G, BIO-RAD, Hercules, CA), iNOS (dilution 1:200; PA3-030A, Thermo Fisher Scientific), and CD206 (dilution 1:200; PA5-46994, Thermo Fisher Scientific). Alexa Fluor-conjugated secondary antibodies (Donkey Anti rat-AlexaFluor 488, Donkey Anti rabbit-AlexaFluor 647, Donkey Anti goat-AlexaFluor 568, dilution 1:200, Thermo Fisher Scientific) were used for subsequent staining, followed by counterstaining with DAPI. To preserve the samples, an anti-fade mountant (SlowFade Mountant; S36936, Thermo Fisher Scientific) was applied, and imaging was performed using a high-resolution microscope (BX-X800, KEYENCE, Itasca, IL). For each sample, five randomly selected fields at the wound centre were imaged, which was determined by the absence of epidermal structures, which were confirmed by parallel Haematoxylin and Eosin (H&E) staining of consecutive sections. The acquired images were subjected to processing using ImageJ and Cell-Profiler 4.2 software for semi-quantitative analysis. The numbers of macrophage subtypes were manually counted based on double-positive staining through blind counting for reducing statistical bias.

ACKNOWLEDGMENTS

This research is sponsored by the Defense Advanced Research Projects Agency (DARPA) through Cooperative Agreement D20AC00003 awarded by the U.S. Department of the Interior (DOI), Interior Business Center. The content of the information does not necessarily reflect the position or the policy of the Government, and no official endorsement should be inferred.

CONFLICT OF INTEREST STATEMENT

The authors declare no conflicts of interest.

DATA AVAILABILITY STATEMENT

The data that support the findings of this study are available from the corresponding author upon reasonable request.

ORCID

Narges Asefifeyzabadi  <https://orcid.org/0009-0003-0872-0299>

Hsin-ya Yang  <https://orcid.org/0000-0002-5325-494X>

Maryam Tebyani  <https://orcid.org/0000-0001-5477-2805>

Michael Levin  <https://orcid.org/0000-0001-7292-8084>

Min Zhao  <https://orcid.org/0000-0002-2500-3035>

Roslyn Rivkah Isseroff  <https://orcid.org/0000-0001-7813-0858>

REFERENCES

- Demidova-Rice TN, Hamblin MR, Herman IM. Acute and impaired wound healing: pathophysiology and current methods for drug delivery, part 1: normal and chronic wounds: biology, causes, and approaches to care. *Adv Skin Wound Care*. 2012;25(7):304-314.
- Wang C, Jiang X, Kim HJ, et al. Flexible patch with printable and anti-bacterial conductive hydrogel electrodes for accelerated wound healing. *Biomaterials*. 2022;285:121479.
- Selberg J, Gomez M, Rolandi M. The potential for convergence between synthetic biology and bioelectronics. *Cell Syst*. 2018;7(3):231-244.
- Yuk H, Lu B, Zhao X. Hydrogel bioelectronics. *Chem Soc Rev*. 2019;48(6):1642-1667.
- Shaner S, Savelyeva A, Kvartuh A, et al. Bioelectronic microfluidic wound healing: a platform for investigating direct current stimulation of injured cell collectives. *Lab Chip*. 2023;23(6):1531-1546.
- Yu R, Zhang H, Guo B. Conductive biomaterials as bioactive wound dressing for wound healing and skin tissue engineering. *Nano-Micro Lett*. 2021;14(1):1.
- Jia M, Ray S, Breault R, Rolandi M. Control of pH in bioelectronics and applications. *APL Mater*. 2020;8(12):120704.
- Mahanta AK, Senapati S, Paliwal P, Krishnamurthy S, Hemalatha S, Maiti P. Nanoparticle-induced controlled drug delivery using chitosan-based hydrogel and scaffold: application to bone regeneration. *Mol Pharm*. 2019;16(1):327-338.
- Obara K, Ishihara M, Ishizuka T, et al. Photocrosslinkable chitosan hydrogel containing fibroblast growth factor-2 stimulates wound healing in healing-impaired db/db mice. *Biomaterials*. 2003;24(20):3437-3444.
- Panwar V, Babu A, Sharma A, et al. Tunable, conductive, self-healing, adhesive and injectable hydrogels for bioelectronics and tissue regeneration applications. *J Mater Chem B*. 2021;9(31):6260-6270.
- Dargaville TR, Farrugia BL, Broadbent JA, Pace S, Upton Z, Voelcker NH. Sensors and imaging for wound healing: a review. *Bio-sens Bioelectron*. 2013;41:30-42.
- Dechiraju H, Selberg J, Jia M, et al. On-chip on-demand delivery of K⁺ for in vitro bioelectronics. *AIP Adv*. 2022;12(12):125205.
- Isaksson J, Kjäll P, Nilsson D, Robinson N, Berggren M, Richter-Dahlfors A. Electronic control of Ca²⁺ signalling in neuronal cells using an organic electronic ion pump. *Nat Mater*. 2007;6(9):673-679.
- Chesler M. Regulation and modulation of pH in the brain. *Physiol Rev*. 2003;83(4):1183-1221.
- Tybrandt K, Larsson KC, Kurup S, et al. Translating electronic currents to precise acetylcholine-induced neuronal signaling using an organic electrophoretic delivery device. *Adv Mater*. 2009;21(44):4442-4446.
- Williamson A, Rivnay J, Kergoat L, et al. Controlling Epileptiform activity with organic electronic ion pumps. *Adv Mater*. 2015;27(20):3138-3144.
- Simon DT, Kurup S, Larsson KC, et al. Organic electronics for precise delivery of neurotransmitters to modulate mammalian sensory function. *Nat Mater*. 2009;8(9):742-746.
- Jia M, Jafari M, Pansodtee P, Teodorescu M, Gomez M, Rolandi M. A multi-ion electrophoretic pump for simultaneous on-chip delivery of H⁺, Na⁺, and Cl⁻. *APL Mater*. 2022;10(4):041112.

19. Linju MC, Rekha MR. Role of inorganic ions in wound healing: an insight into the various approaches for localized delivery. *Ther Deliv*. 2023;14(10):649-667.
20. Nagoba BS, Gandhi RC, Wadher BJ, Potekar RM, Kolhe SM. Microbiological, histopathological and clinical changes in chronic infected wounds after citric acid treatment. *J Med Microbiol*. 2008;57(Pt 5):681-682.
21. Nagoba B et al. Acidic environment and wound healing: a review. *Wounds*. 2015;27:5-11.
22. Kruse CR, Singh M, Targosinski S, et al. The effect of pH on cell viability, cell migration, cell proliferation, wound closure, and wound reepithelialization: in vitro and in vivo study. *Wound Repair Regen*. 2017;25(2):260-269.
23. Stock C. pH-regulated single cell migration. *Pflugers Arch*. 2024;476(4):639-658.
24. Sim P, Strudwick XL, Song YM, Cowin AJ, Garg S. Influence of acidic pH on wound healing in vivo: a novel perspective for wound treatment. *Int J Mol Sci*. 2022;23(21):13655.
25. Schneider LA, Korber A, Grabbe S, Dissemmond J. Influence of pH on wound-healing: a new perspective for wound-therapy? *Arch Dermatol Res*. 2007;298(9):413-420.
26. Mai K, Maverakis E, Li J, Zhao M. Maintaining and restoring gradients of ions in the epidermis: the role of ion and water channels in acute cutaneous wound healing. *Adv Wound Care (New Rochelle)*. 2023;12(12):696-709.
27. Denda M, Inoue K, Inomata S, Denda S. Gamma-aminobutyric acid (a) receptor agonists accelerate cutaneous barrier recovery and prevent epidermal hyperplasia induced by barrier disruption. *J Invest Dermatol*. 2002;119(5):1041-1047.
28. Han D, Kim HY, Lee HJ, Shim I, Hahm DH. Wound healing activity of gamma-aminobutyric acid (GABA) in rats. *J Microbiol Biotechnol*. 2007;17(10):1661-1669.
29. Arribas-López E, Zand N, Ojo O, Snowden MJ, Kochhar T. The effect of amino acids on wound healing: a systematic review and meta-analysis on arginine and glutamine. *Nutrients*. 2021;13(8):2498.
30. Thangavel P, Ramachandran B, Chakraborty S, Kannan R, Lonchin S, Muthuvijayan V. Accelerated healing of diabetic wounds treated with L-glutamic acid loaded hydrogels through enhanced collagen deposition and angiogenesis: an in vivo study. *Sci Rep*. 2017;7(1):10701.
31. Kesici U, Kesici S, Ulusoy H, et al. Effects of glutamine on wound healing. *Int Wound J*. 2015;12(3):280-284.
32. Uberty F, Morsanuto V, Ghirlanda S, et al. Highly diluted acetylcholine promotes wound repair in an in vivo model. *Adv Wound Care (New Rochelle)*. 2018;7(4):121-133.
33. Sadiq A, Shah A, Jeschke M, et al. The role of serotonin during skin healing in post-thermal injury. *Int J Mol Sci*. 2018;19(4):1034.
34. Blackiston DJ, Anderson GM, Rahman N, Bieck C, Levin M. A novel method for inducing nerve growth via modulation of host resting potential: gap junction-mediated and serotonergic signaling mechanisms. *Neurotherapeutics*. 2015;12(1):170-184.
35. Mehta AS et al. Quantifying innervation facilitated by deep learning in wound healing. *Res Sq*. 2023;13(1):16885.
36. Blackiston DJ, Vien K, Levin M. Serotonergic stimulation induces nerve growth and promotes visual learning via posterior eye grafts in a vertebrate model of induced sensory plasticity. *NPJ Regen Med*. 2017;2(1):8.
37. Hoffmann O, Keilwerth N, Bille MB, et al. Triptans reduce the inflammatory response in bacterial meningitis. *J Cereb Blood Flow Metab*. 2002;22(8):988-996.
38. Döring K, Best C, Birklein F, Krämer HH. Zolmitriptan inhibits neurogenic inflammation and pain during electrical stimulation in human skin. *Eur J Pain*. 2015;19(7):966-972.
39. Fregoso DR, Hadian Y, Gallegos AC, et al. Skin-brain axis signaling mediates behavioral changes after skin wounding. *Brain Behav Immun—Health*. 2021;15:100279.
40. Zhao M, Song B, Pu J, et al. Electrical signals control wound healing through phosphatidylinositol-3-OH kinase-gamma and PTEN. *Nature*. 2006;442(7101):457-460.
41. Sun Y, Reid B, Ferreira F, et al. Infection-generated electric field in gut epithelium drives bidirectional migration of macrophages. *PLoS Biol*. 2019;17(4):e3000044.
42. Love MR, Palee S, Chattipakorn SC, Chattipakorn N. Effects of electrical stimulation on cell proliferation and apoptosis. *J Cell Physiol*. 2018;233(3):1860-1876.
43. Comerici CJ, Gillman AL, Galera-Laporta L, et al. Localized electrical stimulation triggers cell-type-specific proliferation in biofilms. *Cell Syst*. 2022;13(6):488-498.e4.
44. Xu K, Liu X, Li X, et al. Effect of electrical and electromechanical stimulation on PC12 cell proliferation and axon outgrowth. *Front Bioeng Biotechnol*. 2021;9:757906.
45. Enayati S, Chang K, Achour H, et al. Electrical stimulation induces retinal Müller cell proliferation and their progenitor cell potential. *Cells*. 2020;9(3):781.
46. Zhao S, Mehta AS, Zhao M. Biomedical applications of electrical stimulation. *Cell Mol Life Sci*. 2020;77(14):2681-2699.
47. Zheng T, Zhang Z, Zhu R, Sun D. A microelectrode array chip for osteogenic differentiation of mesenchymal stem cells under electrical stimulation. *Lab Chip*. 2020;20(2):373-383.
48. Lim PLK et al. Automated electrical stimulation therapy accelerates Re-epithelialization in a three-dimensional in vitro human skin wound model. *Adv Wound Care (New Rochelle)*. 2024.
49. Guo R, Liu J. Implantable liquid metal-based flexible neural microelectrode array and its application in recovering animal locomotion functions. *J Micromech Microeng*. 2017;27(10):104002.
50. Miranda I, Souza A, Sousa P, et al. Properties and applications of PDMS for biomedical engineering: a review. *J Funct Biomater*. 2022;13(1):2.
51. Baniya P, Tebyani M, Asefifeyzabadi N, et al. A system for bioelectronic delivery of treatment directed toward wound healing. *Sci Rep*. 2023;13(1):14766.
52. Jia M, Luo L, Rolandi M. Correlating ionic conductivity and microstructure in polyelectrolyte hydrogels for bioelectronic devices. *Macromol Rapid Commun*. 2022;43(6):2100687.
53. Vasile E, Ciocanea A, Ionescu V, Lepadatu I, Diac C, Stamatin SN. Making precious metals cheap: a sonoelectrochemical - hydrodynamic cavitation method to recycle platinum group metals from spent automotive catalysts. *Ultrason Sonochem*. 2021;72:105404.
54. Nguyen T, Asefifeyzabadi N, Li H, Luo L, Rolandi M. The importance of electrode material in bioelectronic electrophoretic ion pumps. *Adv Mater Technol*. 2023;8:2201996.
55. Bard AJ, Jordan RPJ. *Standard Potentials in Aqueous Solution*. 1985.
56. Waldherr L, Seitanidou M, Jakešová M, et al. Targeted chemotherapy of glioblastoma spheroids with an Iontronic pump. *Adv Mater Technol*. 2021;6(5):2001302.
57. Uguz I, Proctor CM, Curto VF, et al. A microfluidic ion pump for in vivo drug delivery. *Adv Mater*. 2017;29(27):1701217.
58. Žuržul N, Ilseng A, Prot VE, Sveinsson HM, Skallerud BH, Stokke BT. Donnan contribution and specific ion effects in swelling of cationic hydrogels are additive: combined high-resolution experiments and finite element modeling. *Gels*. 2020;6(3):31.
59. Yoon DJ, Nguyen C, Bagood MD, et al. Topical fluoxetine as a potential nonantibiotic adjunctive therapy for infected wounds. *J Invest Dermatol*. 2021;141(6):1608-1612.e3.
60. Bennison L et al. The pH of wounds during healing and infection: a descriptive literature review. *Wound Pract Res*. 2017;25:63.
61. Percival SL, McCarty S, Hunt JA, Woods EJ. The effects of pH on wound healing, biofilms, and antimicrobial efficacy. *Wound Repair Regen*. 2014;22(2):174-186.



62. Liu Y, Kalén A, Risto O, Wahlström O. Fibroblast proliferation due to exposure to a platelet concentrate in vitro is pH dependent. *Wound Repair Regen.* 2002;10(5):336-340.
63. Tai G, Tai M, Zhao M. Electrically stimulated cell migration and its contribution to wound healing. *Burns Trauma.* 2018;6:20.
64. Krzyszczyk P, Schloss R, Palmer A, Berthiaume F. The role of macrophages in acute and chronic wound healing and interventions to promote pro-wound healing phenotypes. *Front Physiol.* 2018;9:419.
65. Lucas T, Waisman A, Ranjan R, et al. Differential roles of macrophages in diverse phases of skin repair. *J Immunol.* 2010;184(7):3964-3977.
66. Mosser DM, Edwards JP. Exploring the full spectrum of macrophage activation. *Nat Rev Immunol.* 2008;8(12):958-969.
67. Li H et al. Programmable delivery of fluoxetine via wearable bioelectronics for wound healing in vivo. *Adv Mater Technol.* 2024;9:2301115.
68. Aitcheson SM, Frentiu FD, Hurn SE, Edwards K, Murray RZ. Skin wound healing: normal macrophage function and macrophage dysfunction in diabetic wounds. *Molecules.* 2021;26(16):4917.
69. Tavakoli S et al. Immunomodulation of skin repair: cell-based therapeutic strategies for skin replacement (a comprehensive review). *Bio-medicine.* 2022;10(1):118.

SUPPORTING INFORMATION

Additional supporting information can be found online in the Supporting Information section at the end of this article.

How to cite this article: Asefifeyzabadi N, Nguyen T, Li H, et al. A pro-reparative bioelectronic device for controlled delivery of ions and biomolecules. *Wound Rep Reg.* 2024;32(5): 709-719. doi:[10.1111/wrr.13191](https://doi.org/10.1111/wrr.13191)